Title

Numerical Study of Bond and Development of Column Longitudinal Reinforcement Extended into Oversized Pile Shafts

Permalink

https://escholarship.org/uc/item/86k2h0c5

Authors

Murcia-Delso, Juan
Shing, P Benson

Peer reviewed

Numerical Study of Bond and Development of Column Longitudinal Reinforcement Extended into Oversized Pile Shafts

Juan Murcia-Delso[1] and P. Benson Shing, M.ASCE[2]

Abstract: This paper presents a numerical investigation to examine the bond-slip behavior of column longitudinal reinforcing bars embedded in oversized pile shafts and to determine the minimum embedment length required for the column bars to prevent anchorage failure. Three-dimensional nonlinear finite-element models of column-pile assemblies incorporating the bond-slip behavior of the longitudinal reinforcing bars have been developed for the numerical analyses. The capability of the models in capturing the response of column bars along their embedment length has been verified with experimental results from four full-scale column-pile assemblies tested under cyclic lateral loads. The study has shown that the bond-stress distribution along the bar anchorage length is highly nonuniform and that the embedment length specified for the column reinforcement in current design standards is very conservative. A new design formula that significantly reduces the embedment length has been evaluated. The numerical results have indicated that the new embedment-length formula provides a good margin of safety against the pull-out failure of the column bars. The results have also shown that the use of an engineered steel casing to provide lateral confinement for the pile is an effective means to enhance the bond strength and reduce the slip of the column longitudinal bars in the anchorage region. **DOI: [10.1061/(ASCE)ST.1943-541X.0002024](#).** *© 2018 American Society of Civil Engineers.*

Introduction

Cast-in-drilled-hole piles are frequently used in bridges because of the construction efficiency and reduced footprints as compared with other types of foundations. In seismic regions, oversized pile shafts (i.e., pile shafts having a larger cross section than the columns they support) are often preferred over those that have the same cross-sectional dimensions as the columns, because they ensure that plastic hinging always occurs in the columns above the pile shafts, which is more convenient for postearthquake inspection and repair. However, because of their different cross sections, the column and the pile must have discontinuous reinforcement cages, and the column longitudinal reinforcement has to form a noncontact lap splice with the longitudinal reinforcement of the pile. The seismic design criteria of the California Department of Transportation (Caltrans 2010) and the AASHTO LRFD seismic bridge design specifications (SBDS) (AASHTO 2011) require that column longitudinal bars extended into oversized pile shafts be terminated in a staggered manner with minimum embedment lengths of $D_{c,\max} + l_d$ and $D_{c,\max} + 2l_d$, respectively, where $D_{c,\max}$ is the larger cross-sectional dimension of the column, and l_d is the development length required for a straight bar in tension based on the expected material properties.

The Caltrans and AASHTO requirements presented previously can be regarded as very conservative based on the results of laboratory tests conducted by Murcia-Delso et al. (2016) on four large-scale column-pile assemblies and those carried out by McLean and Smith (1997) on smaller specimens. Murcia-Delso et al. (2016) have shown that an embedment length of $l_d + s + c$ is sufficient to develop the tensile strength of the longitudinal reinforcement in the columns, where l_d is the development length in tension according to the AASHTO LRFD bridge design specifications (BDS) (AASHTO 2010) and AASHTO LRFD SBDS (AASHTO 2011), whichever governs; s is the center-to-center spacing between the column and the pile longitudinal steel; and c is the thickness of the concrete cover at the top of the pile. This embedment length is significantly shorter than that required in the Caltrans (2010) and AASHTO (2011) specifications, and that recommended by McLean and Smith (1997). Nevertheless, the experimental data do not provide sufficient information to establish the margin of safety against bar anchorage failure for this reduced embedment length.

This paper presents a numerical study conducted with nonlinear finite element (FE) models to further the understanding of the bond-slip behavior and the development of column longitudinal reinforcement in oversized pile shafts. The FE models used in this study have the bond-slip behavior represented by a constitutive model developed by Murcia-Delso and Shing (2015). The constitutive model has been implemented in an interface element and validated with experimental data from bond-slip and development-length tests (Murcia-Delso and Shing 2015; Murcia-Delso et al. 2015). The FE models presented in this paper have been verified with experimental results from four large-scale column-pile assemblies tested by Murcia-Delso et al. (2016) to study the adequacy of the anchorage capacity of column reinforcement embedded in enlarged pile shafts. These models yield quantitative information on the bar stress, bond stress, and bar slip along the bar anchorage region of the test specimens, which could not be measured in the tests but is crucial for identifying the margin of safety against bar anchorage failure. Additional FE analyses have been conducted to confirm that the embedment length calculated with the formula

[1]Assistant Professor, Dept. of Civil, Architectural and Environmental Engineering, Univ. of Texas, Austin, TX 78712 (corresponding author). E-mail: murcia@utexas.edu

[2]Professor, Dept. of Structural Engineering, Univ. of California, San Diego, La Jolla, CA 92161.

Fig. 1. Column-pile test specimen (reprinted from Murcia-Delso et al. 2016, © ASCE)

proposed by Murcia-Delso et al. (2016) provides an adequate safety margin for columns and piles with different cross-sectional dimensions, different longitudinal reinforcement ratios, and bar sizes, which could be encountered in bridge structures.

Full-Scale Column-Pile Tests

The column-pile assembly tests (Murcia-Delso et al. 2016) used to verify the FE models are briefly summarized here. Four full-scale specimens consisting of a bridge column and the upper portion of a pile shaft, like that shown in Fig. 1, were tested under fully reversed cyclic lateral loading. The main properties of the specimens are given in Table 1. The columns in these specimens had a diameter of 1,219 mm (4 ft) and aspect ratios varying between 4 and 4.5. Specimens 1–3 had 1,829-mm (6-ft) diameter piles, and the fourth had a 1,524-mm (5-ft) diameter pile. The specimens were designed according to Caltrans practice, except for the embedment length of the column reinforcement inside the pile and the transverse reinforcement in the anchorage region of the pile.

Specimen 1 had an embedment length equal to $D_{c,\max} + l_d$. The requirement to terminate half of the longitudinal bars at $D_{c,\max} + 2l_d$ was not followed, as it was proved to be safe by a pretest FE analysis of the column-pile assembly. Specimens 2 to 4 had shorter embedment lengths of $l_d + s + c$. The transverse reinforcement in the pile of Specimen 1 was based on the AASHTO LRFD BDS (AASHTO 2011) design requirements for compression members, whereas those of Specimens 2 and 4 were based on formulas proposed by McLean and Smith (1997) and Murcia-Delso et al. (2016), respectively, to prevent premature bar anchorage failure that could be caused by concrete splitting. Specimen 3 was similar to Specimen 2, but had a steel casing around the pile. The thickness of the casing was determined with a more stringent criterion proposed by Murcia-Delso et al. (2016) to limit the width of tensile-splitting cracks in the pile. The resulting amount of transverse reinforcement in each specimen is presented in Table 1.

The concrete for the piles and columns had a specified compressive strength of 31 MPa (4,500 psi) at 28 days, and the specimens were tested when the concrete strengths in the column and the pile were close to 34.5 MPa (5,000 psi). The reinforcing steel was Grade 60, complying with the ASTM A706 (ASTM 2009) standards. The sizes and amounts of longitudinal and transverse reinforcement are given in Table 1. The steel casing of Specimen

Table 1. Test Specimens and FE Models of Column-Pile Assemblies

Model identifier (test specimen number)	Column diameter [mm (ft)]	Pile diameter [mm (ft)]	Column height [mm (ft)]	Pile height [mm (ft)]	Column longitudinal reinforcement (reinforcement ratio)	Pile longitudinal reinforcement (reinforcement ratio)	$\rho_{v,\text{pile}}$[a] (%)	Formula for l_e	l_e [mm (ft)]
1a (1)	1,219 (4)	1,829 (6)	4,877 (16)	2,743 (9)	18 No. 11 (1.55%)	28 No. 14 (1.55%)	0.82[b]	$D_{c,\max} + l_d$	2,286 (7.5)
1b							1.07[c]	$l_d = s + c$	1,422 (4.67)
1c							1.07[c]	$0.7l_d$	762 (2.5)
2a (2)	1,219 (4)	1,829 (6)	5,486 (18)	2,439 (8)	18 No. 14 (2.24%)	26 No. 18 (2.55%)	1.04[d]	$l_d + s + c$	1,829 (6)
2b								$0.65l_d$	940 (3.1)
3 (3)	1,219 (4)	1,829 (6)	5,486 (18)	2,439 (8)	18 No. 14 (2.24%)	26 No. 18 (2.55%)	1.65[e]	$l_d = s + c$	1,829 (6)
4 (4)	1,219 (4)	1,524 (5)	4,877 (16)	1,829 (6)	32 No. 8 (1.40%)	40 No. 11 (2.21%)	1.62[c]	$l_d = s + c$	940 (3.1)
5a	2,438 (8)	3,048 (10)	9,754 (32)	3,048 (10)	38 No. 14 (1.18%)	48 No. 18 (1.70%)	1.58[c]	$l_d = s + c$	1,829 (6)
5b								$0.75l_d$	1,092 (3.6)
6	2,438 (8)	3,658 (12)	9,754 (32)	3,048 (10)	40 No. 14 (1.24%)	56 No. 18 (1.38%)	1.31[c]	$l_d = s + c$	2,134 (7)
7	2,438 (8)	3,658 (12)	9,754 (32)	3,048 (10)	34 No. 18 (1.88%)	56 No. 18 (1.38%)	1.53[c]	$l_d = s + c$	2,565 (8.4)

Note: No. 5 = 16 mm, No. 6 = 19 mm, No. 7 = 22 mm, No. 8 = 25 mm, No. 11 = 36 mm, No. 14 = 43 mm, and No. 18 = 57 mm.
[a]Volumetric ratio of pile transverse reinforcement in bar anchorage region of pile with respect to confined concrete core: $\rho_{v,\text{pile}} = 4A_{tr}/(D_{s,\text{core}}s_{tr})$.
[b]Transverse reinforcement determined based on the requirement for compression members in Article 5.7.4.6 of the AASHTO LRFD BDS (AASHTO 2010).
[c]Transverse reinforcement determined with the formula proposed by Murcia-Delso et al. (2016).
[d]Transverse reinforcement determined with the formula proposed by McLean and Smith (1997).
[e]Total equivalent amount of Grade 60 transverse steel, based on the crack-width control criterion recommended by Murcia-Delso et al. (2016).

Table 2. Material Properties for Concrete, Longitudinal Steel, and Bond-Slip Models

Model identifier	Region	Concrete and longitudinal reinforcement parameters				Bond-slip parameters		
		f'_c [MPa (ksi)]	d_b [mm (in.)]	f_y [MPa (ksi)]	f_u [MPa (ksi)]	τ_{max} [MPa (ksi)]	s_{peak}	s_R
1a, 1b, 1c	Pile/lap splice region	34.5 (5.0)	43 (1.69)	484 (70.1)	672 (97.4)	16.5 (2.40)	3.0 (0.12)	21.5 (0.85)
	Pile/below lap splice	42.8 (6.2)				19.4 (2.82)		
	Column/lower 2.8 m (9 ft)	34.0 (4.9)	36 (1.41)	448 (65.0)	629 (91.2)	16.3 (2.36)	2.5 (0.10)	18 (0.71)
	Column/upper 2.1 m (7 ft)	38.6 (5.6)				18.0 (2.61)		
2a, 2b	Pile/lap splice region	37.0 (5.4)	57 (2.25)	462 (67.0)	641 (93.0)	17.5 (2.54)	4.0 (0.16)	28.5 (1.13)
	Pile/below lap splice	39.7 (5.8)				18.5 (2.68)		
	Column/lower 2.8 m (9 ft)	38.6 (5.6)	43 (1.69)	462 (67.0)	638 (92.5)	18.0 (2.61)	3.0 (0.12)	21.5 (0.85)
	Column/upper 2.4 m (8 ft)	40.7 (5.9)				18.6 (2.70)		
3	Pile/lap splice region	36.2 (5.3)	57 (2.25)	462 (67.0)	652 (94.5)	17.3 (2.51)	4.0 (0.16)	28.5 (1.13)
	Pile/below lap splice	34.1 (4.9)				16.3 (2.36)		
	Column/lower 2.8 m (9 ft)	35.0 (5.1)	43 (1.69)	462 (67.0)	641 (93.0)	16.7 (2.42)	3.0 (0.12)	21.5 (0.85)
	Column/upper 2.4 m (8 ft)	33.2 (4.8)				16.0 (2.31)		
4	Pile/lap splice region	36.6 (5.3)	36 (1.41)	445 (64.5)	634 (92.0)	17.3 (2.51)	2.5 (0.10)	18 (0.71)
	Pile/below lap splice	33.0 (4.8)				16.0 (2.31)		
	Column/lower 2.8 m (9 ft)	35.5 (5.1)	25 (1.0)	459 (66.5)	650 (94.3)	16.7 (2.42)	1.8 (0.07)	12.5 (0.5)
	Column/upper 2.1 m (7 ft)	33.9 (4.9)				16.3 (2.36)		
5a, 5b	Pile	34.5 (5.0)	57 (2.25)	469 (68)	655 (95.0)	16.5 (2.40)	4.0 (0.16)	28.5 (1.13)
6	Column		43 (1.69)				3.0 (0.12)	21.5 (0.85)
7	Pile and column	34.5 (5.0)	57 (2.25)	469 (68)	655 (95.0)	16.5 (2.40)	4.0 (0.16)	28.5 (1.13)

3 was 6.4-mm (0.25-in.) thick and was made of A36 steel. The actual strengths of the concrete obtained on the same days as the column-pile tests and the strengths of the reinforcing steel, which are used to calibrate the FE models, are presented in Table 2.

The test specimens were loaded under a constant vertical load that subjected the base of the column to an axial stress equal to 9.4% of the target compressive strength of 34.5 MPa (5,000 psi) for the concrete. The top of the column was subjected to cyclic lateral displacements in the north–south direction using two servo-controlled hydraulic actuators reacting against a strong wall. The lateral loading protocol consisted of four fully reversed force-controlled load cycles of increasing amplitudes up to the theoretical first yield of the column longitudinal reinforcement, and then fully reversed displacement-controlled load cycles of increasing ductility demands (with two cycles for each displacement amplitude) up to failure. The ductility demand is defined as $\mu = \Delta/\Delta_y$, in which Δ is the lateral displacement of the specimen (measured at the elevation of the center line of the horizontal actuators), and Δ_y is the effective yield displacement of an equivalent elastic-perfectly plastic system as defined in Murcia-Delso et al. (2016).

All of the specimens behaved in a ductile manner with plastic hinges developing at the base of the columns, as shown in Fig. 2. Failure was characterized by the spalling of concrete near the column base and the buckling and fracture of the longitudinal bars at high displacement levels. Damage in the piles was primarily radial cracks caused by the splitting forces induced by bar slip and the prying action of the columns. Circular cracks were also observed on the top surface of the piles. The degree of damage in the piles varied among the specimens, with the most severe splitting cracks observed in Specimens 2 and 4, and the least damage observed in Specimen 3 owing to the additional confinement provided by the steel casing. The damage observed at the top of the piles of Specimens 2 and 3 is shown in Fig. 2. The test data are compared with the FE analysis results in a later section.

Fig. 2. Damage in the column-pile specimens at the end of testing (reprinted from Murcia-Delso et al. 2016, © ASCE): (a) Specimen 2; (b) Specimen 3
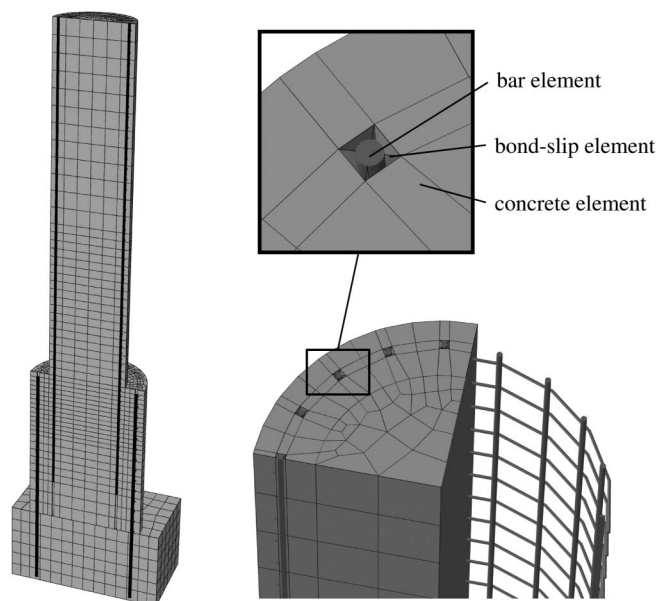
Fig. 3. Finite-element model of a column-pile assembly

Table 3. Calibration of Strength-Independent Parameters of Damage-Plastic Model

Parameter	Definition	Value
α	Parameter controlling biaxial compressive strength	0.12
φ	Dilation angle	20°
γ	Parameter controlling shape of the yield surface	1.91
w_c	Compression recovery factor	0
w_t	Tension recovery factor	1

Finite-Element Modeling of Column-Pile Assemblies

Three-dimensional nonlinear FE models of the column-pile specimens tested in the laboratory have been developed with the program *Abaqus*. Fig. 3 shows the model for one of the specimens. Only one-half of the specimen is modeled by taking advantage of the symmetry plane in the north–south (loading) direction. In the following discussion, south is defined as the positive direction. Concrete and steel reinforcement are modeled with constitutive laws available in *Abaqus*. Beam elements are used to represent the longitudinal bars. Beam elements are connected to concrete solid elements through interface elements to capture the bond-slip behavior of the longitudinal reinforcement, as shown in Fig. 3. The bond-slip interface element has been developed and implemented in *Abaqus* with a user-programmed subroutine by Murcia-Delso

and Shing (2015). Perfect bond is assumed for the transverse reinforcement, which is modeled with truss elements embedded in the concrete elements. The steel casing of Specimen 3 is modeled with shell elements and the same constitutive law as the reinforcing steel. Geometric nonlinearity is considered.

Concrete Model

The damage-plasticity constitutive model available in *Abaqus*, which is based on the formulations proposed by Lubliner et al. (1989) and Lee and Fenves (1998), is used for concrete. The calibration of the material parameters of the damage-plasticity model is described in Murcia-Delso et al. (2013). The parameters governing the strength of concrete are determined with the material test data given in Table 2. The rest of parameters are presented in Table 3.

In compression, the required stress-strain relations have been determined based on the uniaxial law for unconfined concrete proposed by Karthik and Mander (2011) and the compressive strengths provided in Table 2. The damage-plasticity model is capable of reproducing the effect of the lateral confinement on the compressive strength and lateral dilatation of concrete. However, as discussed in Murcia-Delso et al. (2013), the model is not able to account for the increase of ductility in compression provided by the lateral confinement, which is an important consideration for the modeling the behavior of the plastic-hinge region of a reinforced concrete column. To overcome this limitation, the postpeak slope of the uniaxial compressive stress-strain curve for the confined concrete cores of the columns and the piles are specified a priori based on the amount of confining steel, as shown in Fig. 4(a). The postpeak slope is determined from the uniaxial law for confined concrete proposed by Karthik and Mander (2011).

In tension, the concrete model cannot handle the large stiffness degradation required to accurately represent the cyclic response of cracks, as discussed in Murcia-Delso et al. (2013) and Moharrami and Koutromanos (2016). Hence, after the development of a widely opened crack, the model can result in a large residual crack opening after unloading. To improve the simulation of the closing of severe flexural cracks expected at the column-pile interface, a discrete crack, whose behavior is governed by specified contact conditions, is introduced at this interface. A discrete crack is also introduced at the pile-footing interface. Although this approach ignores the cohesive strength of concrete, it is deemed acceptable given that flexural cracks will appear at these locations during early stages of loading, as shown in the tests of Murcia-Delso et al. (2016).

Steel Model

Reinforcing steel is modeled using beam and truss elements with an elastoplastic constitutive law with linear kinematic hardening. The yield strength and postyield slope of the model have been calibrated to represent the experimental stress-strain relations obtained from
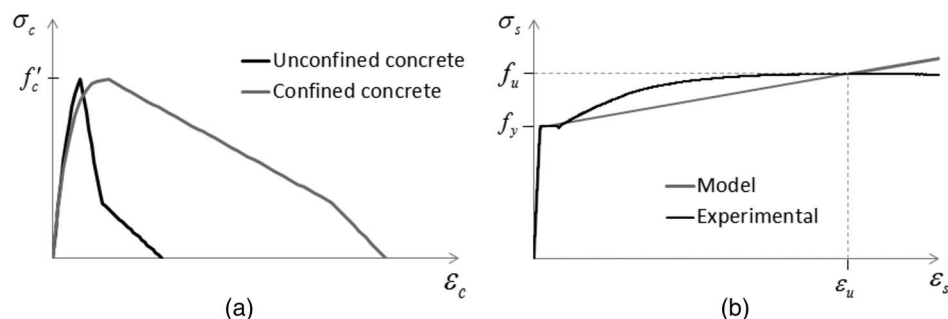

Fig. 4. Calibration of concrete and steel models: (a) input compression stress-strain curves for concrete model; (b) stress-strain curves for steel
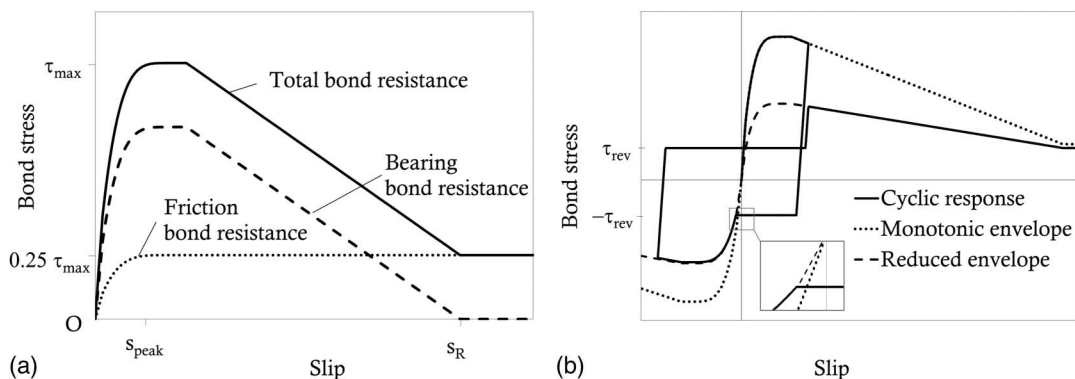
Fig. 5. Bond-slip model (reprinted from Murcia-Delso and Shing 2015, © ASCE): (a) monotonic response; (b) cyclic response

material testing in an approximate manner, as shown in Fig. 4(b). The yield and tensile strengths of the steel are presented in Table 2. Bar fracture is not accounted for in the model.

Bond-Slip Model

The bond-slip behavior of the longitudinal reinforcement is modeled with interface elements that have the constitutive model proposed by Murcia-Delso and Shing (2015). The model accounts for the bond deterioration caused by cyclic slip reversals and the tension yielding of the bar, and the radial stress exerted on the adjacent concrete by the bar ribs as slip occurs. The main features of the bond-slip model are briefly summarized here.

For monotonic loading, the bond stress is expressed as the sum of the bond resistance resulting from the bearing of the bar ribs on concrete (τ_b) and the bond resistance resulting from the friction between the steel and concrete (τ_f). Bond deterioration is governed by a set of strength reduction factors (ρ_i) as follows:

$$\tau(s) = \rho_n(\rho_{b,y} \cdot \rho_{b,c} \cdot \tau_b(s) + \rho_{f,y} \cdot \rho_{f,c} \cdot \tau_f(s)) \quad (1)$$

where ρ_n = reduction factor that accounts for the opening of splitting cracks in concrete; $\rho_{b,s}$ and $\rho_{f,s}$ account for the reduction of the bearing and friction resistances, respectively, caused by the yielding of the bar in tension; and $\rho_{b,c}$ and $\rho_{f,c}$ account for the deterioration caused by cyclic loading. The stress-slip curves for the bearing, friction, and total bond resistances under monotonic loading are plotted in Fig. 5(a). The curves for the bearing and friction resistances are defined piecewise by polynomial functions in terms of three governing parameters, namely, the peak bond strength (τ_{max}) of an elastic bar, the slip at which the peak strength is attained (s_{peak}), and the clear spacing between the bar ribs (s_R). Fig. 5(b) shows the bond stress–versus–slip relation for cyclic loading. The curve follows Eq. (1) for the initial loading and reloading beyond previously attained maximum slip levels. Immediately after slip reversal, a friction resistance of τ_{rev} is developed in the other direction. Once the maximum slip previously attained in the other direction is reached, the monotonic envelope given by Eq. (1) is re-engaged. The equations to calculate the bond-stress envelopes, deterioration factors, and unloading/reloading for cyclic slip reversals are presented in Murcia-Delso and Shing (2015).

The bond stress–versus–slip relations defined previously govern the tangential behavior of the concrete-steel interface along the longitudinal axis of the bar. The interface element has two additional stress and displacement components that are perpendicular to the bar longitudinal axis: one normal and one transverse tangential. The stress-displacement relations in the normal direction are formulated to account for wedging action of the bar ribs. Assuming

that the resultant bond force has a fixed angle of inclination θ with respect to the longitudinal axis of the bar, the normal stress is proportional to the bond stress with the proportionality constant determined by the angle θ, which is taken as 60° based on the recommendations of Murcia-Delso and Shing (2015). For the transverse tangential direction, a penalty stiffness is introduced to restrain the rotation of the bar about its longitudinal axis.

The bond-slip model requires the calibration of only the three parameters governing the monotonic bond stress–versus–slip envelope: τ_{max}, s_{peak}, and s_R. These parameters are calibrated based on the compressive strength of the concrete (f'_c) and the diameter of the bars (d_b), as described in Murcia-Delso and Shing (2015). Their values are presented in Table 2.

Finite-Element Analysis of Column-Pile Assembly Tests

Global Response

Nonlinear static analyses of the column-pile tests have been conducted with the FE models described in the previous section. The lateral load–versus–drift relations obtained from the FE analyses are compared with the test results in Fig. 6. The FE analyses overestimate the maximum load capacities of the assemblies by 2 to 13%, as presented in Table 4. The gradual decay of the load-carrying capacity with increasing displacement caused by the P-delta effect is well captured, as shown in Fig. 6. However, the sudden load drops observed in the last few cycles of the tests are not reproduced by the FE models, because the material model for the reinforcing bars does not account for bar fracture. The numerical results also show less pinched hysteretic curves in the unloading-reloading cycles as a result of the limitation of the model to accurately simulate the closing of cracks in locations other than the column-pile and pile-footing interfaces. As shown in Fig. 7, the models are able to capture the inelastic mechanisms developed in the column and the piles, such as the flexural cracking, concrete crushing at the base of the columns, bar yielding, bar slip, and radial splitting cracking in the piles.

Strains and Stresses in the Column Longitudinal Bars

Fig. 8 compares the numerical and experimental results on the variation of the tensile strains in the column longitudinal bars at the north face of the specimens. The strains are plotted at the peak displacements of cycles, introducing different ductility demands, μ. The distribution of the strains in the longitudinal reinforcement along the plastic-hinge region of the column shows some
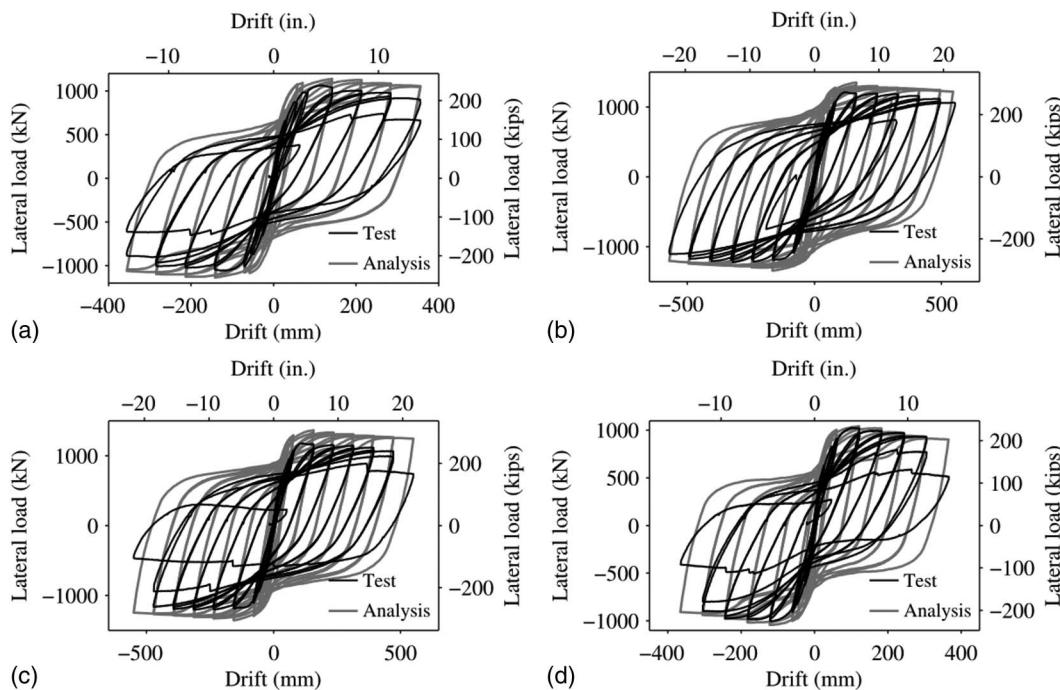
Fig. 6. Lateral force versus drift curves from tests and analyses: (a) Specimen 1; (b) Specimen 2; (c) Specimen 3; (d) Specimen 4

Table 4. Maximum Lateral Load Resistance

Specimen number	Experimental results [kN (kip)]	FE analysis results [kN (kip)]	FE prediction error (%)
Specimen 1	1,063 (239)	1,139 (256)	7
Specimen 2	1,223 (275)	1,348 (303)	10
Specimen 3	1,205 (271)	1,365 (307)	13
Specimen 4	1,023 (230)	1,040 (234)	2

differences with the experimental results when the reinforcement has entered the postyield regime. These differences can be explained by the strong influence of the flexural cracking pattern on the strain distribution in the longitudinal reinforcement (with larger tensile strains localizing at widely opened cracks), in addition to the limitation of the concrete model to accurately represent the closing and re-opening of large cracks in the column during cyclic loading. The agreement between the numerical and experimental results on strain variations along the embedment length of the bars in the pile shafts, which is influenced by the bond-slip behavior, is deemed satisfactory.

Bond deterioration along the anchorage region of the column longitudinal bars can be indirectly assessed from the propagation of plastic tensile strains in the column bars within the pile, which is commonly called plastic strain penetration. As shown in Fig. 8(a), the maximum plastic strain penetration attained in the FE model of Specimen 1 is 0.5 m (1.63 ft), or 14 times the bar diameter d_b, whereas it was 0.61 m (2 ft) or $17d_b$ in the test (occurring at
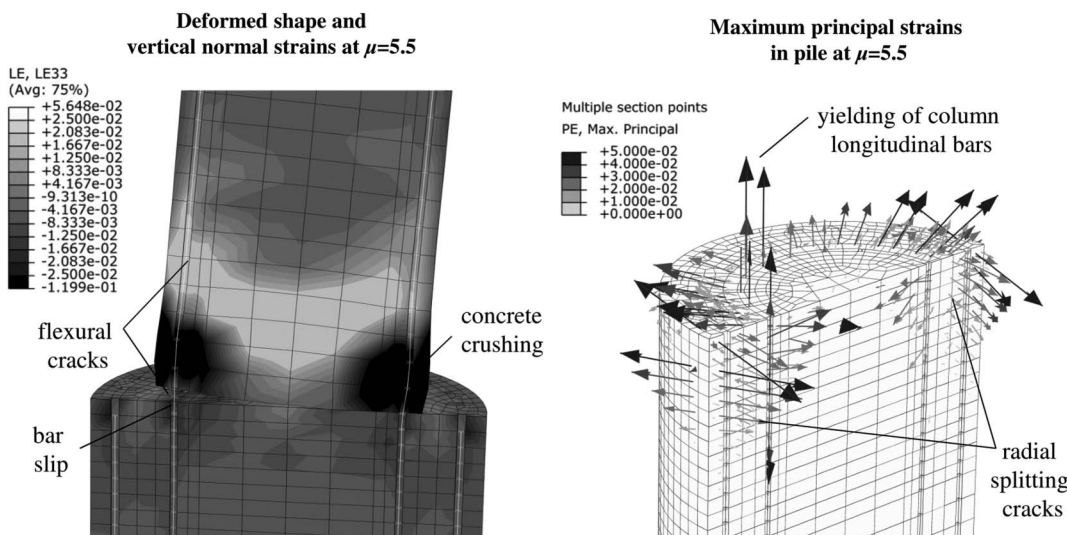
Fig. 7. Inelastic mechanisms predicted by the FE model of Specimen 1
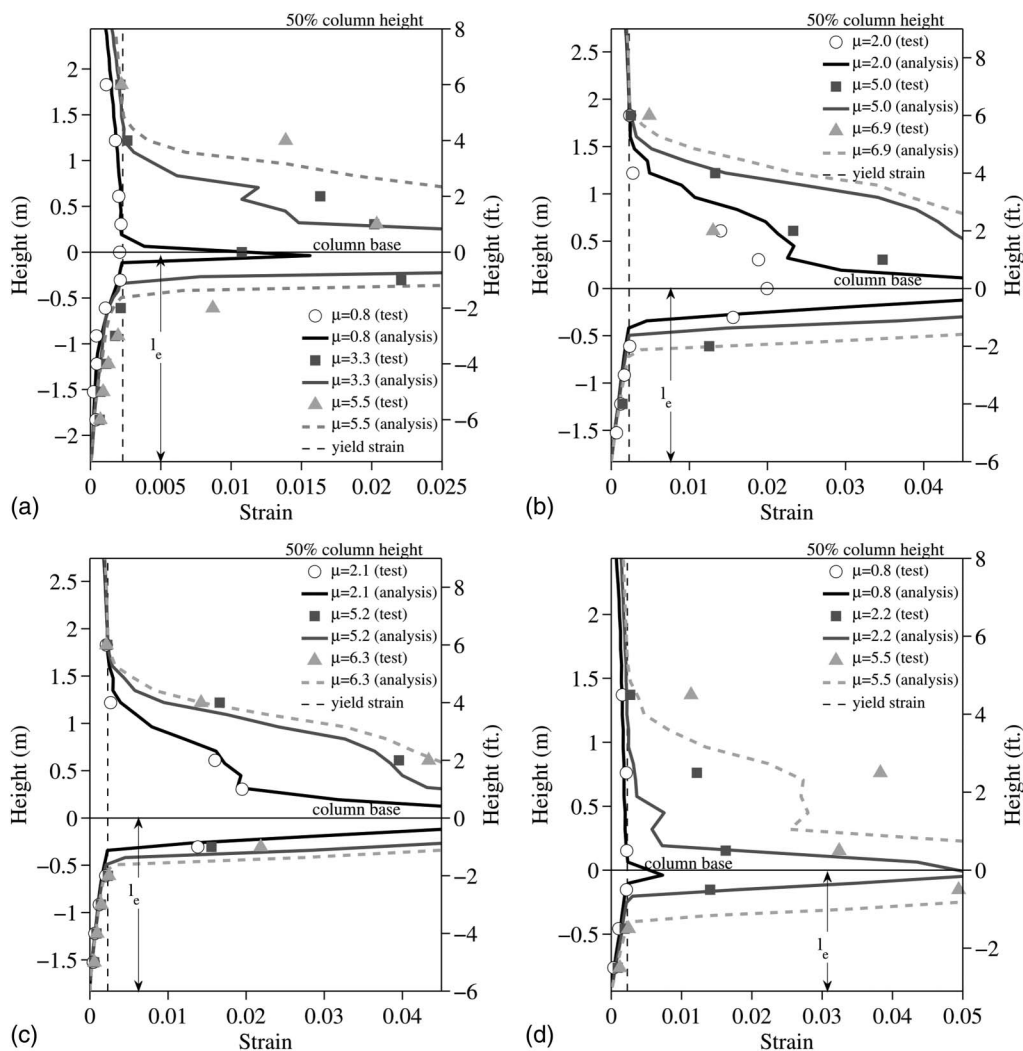
Fig. 8. Tensile strains in the column longitudinal bar at the north face of the specimens: (a) Specimen 1; (b) Specimen 2; (c) Specimen 3; (d) Specimen 4

$\mu = 5.5$, the maximum ductility attained in the test). For Specimens 3 and 4, the maximum plastic strain penetrations obtained with the FE models are $15d_b$ and $16d_b$, respectively, whereas they were $14d_b$ and $18d_b$ in the tests, as shown in Figs. 8(c and d). For Specimen 2, the strain gages were damaged in the last few cycles, and the maximum plastic strain penetration reached could not be measured. According to the FE analysis, it is 0.72 m (2.4 ft) or $17d_b$ occurring at $\mu = 6.0$, as shown in Fig. 8(b).

Fig. 9 plots the tensile stresses developed in the longitudinal bars at the north face of the columns in the FE models of Specimens 1 and 2. The maximum stresses developed in these bars are smaller than the tensile strengths of the bars provided in Table 2. This is consistent with the experimental observations that the fracture of these bars was caused by low-cycle fatigue as a result of severe bending strains induced by bar buckling (Murcia-Delso et al. 2016). However, because bar fracture is not modeled, the failure of the bars is not captured.

Bond-Slip Behavior of Column Longitudinal Bars

The bond stresses along the embedment length of the column bar at the north face of each specimen are plotted in Fig. 10. The stresses are at the peak displacements of different cycles when the bars are in tension. They are compared with the average bond stresses calculated from experimental data obtained from strain gages in the lower portion of the bar anchorage zones in which the bars did not yield. The average bond stress in these regions is calculated as $\tau_{av} = E(\varepsilon_{i+1} - \varepsilon_i)d_b/4L$, where E is the Young's modulus of the steel, and ε_i and ε_{i+1} are strain readings from two adjacent strain gages spaced at a distance L. The agreement between the numerically computed bond stresses and the average bond stresses obtained from the strain gage readings is deemed satisfactory.

For Specimen 1, which had an embedment length of $D_c + l_d$, the bond stresses along the anchorage length are highly nonuniform, as shown in Fig. 10(a). The peak bond stress occurs near the top of the embedment length in the early stages of loading. The peak moves downward as the displacement demand increases, as a result of progressive bond deterioration caused by increased slip and the tensile yielding of the bar at the top of the embedment region. At $\mu = 5.5$, the peak bond stress occurs at 0.53 m (1.75 ft) or $15d_b$ below the column base, practically at the same location as the end of the plastic strain zone shown in Fig. 8. The maximum bond stress attained is 6.9 MPa (1 ksi), which is 40% of the bond strength τ_{max} for an elastic bar. The maximum bond stresses attained are smaller than the bond strength, because the bar section yields before its slip reaches the level required to fully activate τ_{max}.
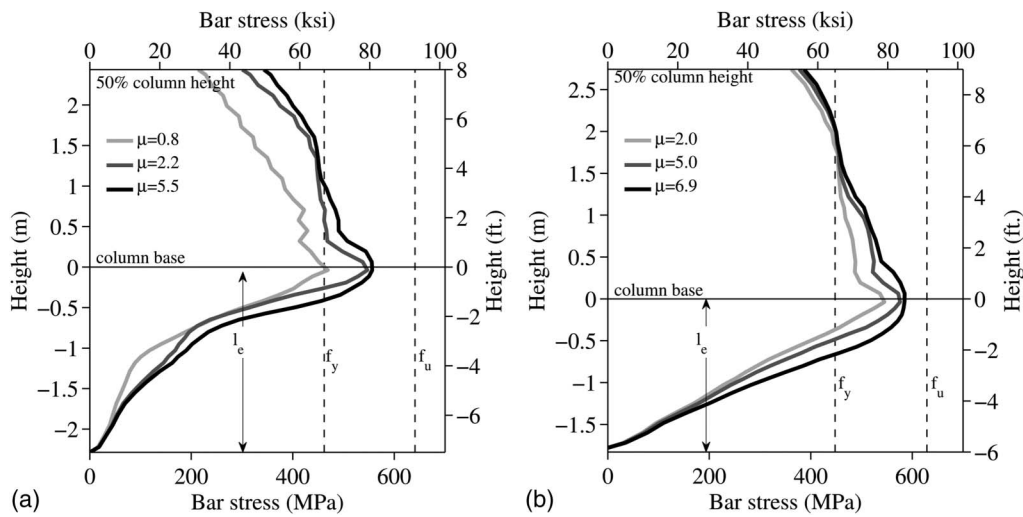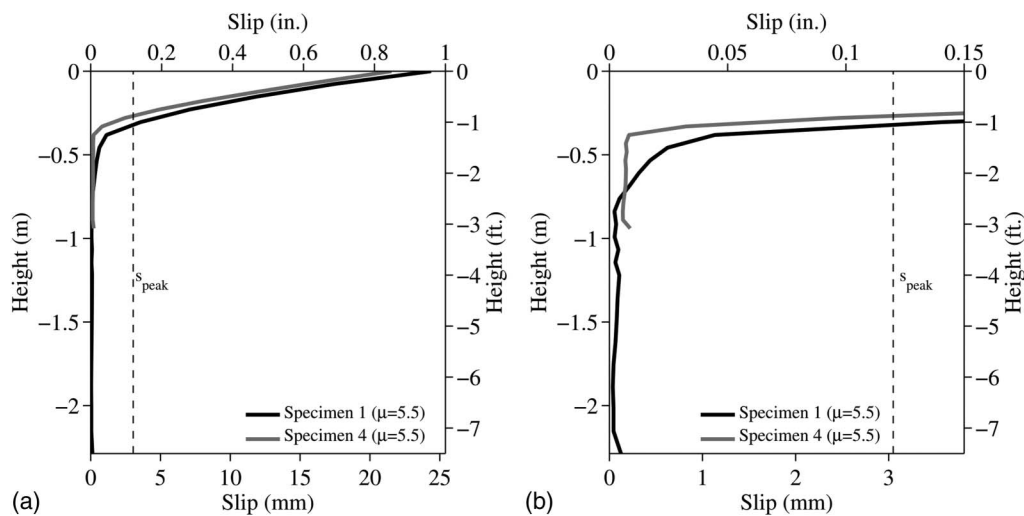
Fig. 9. Tensile stresses in the column longitudinal bar at the north face of the specimens: (a) Specimen 1; (b) Specimen 2
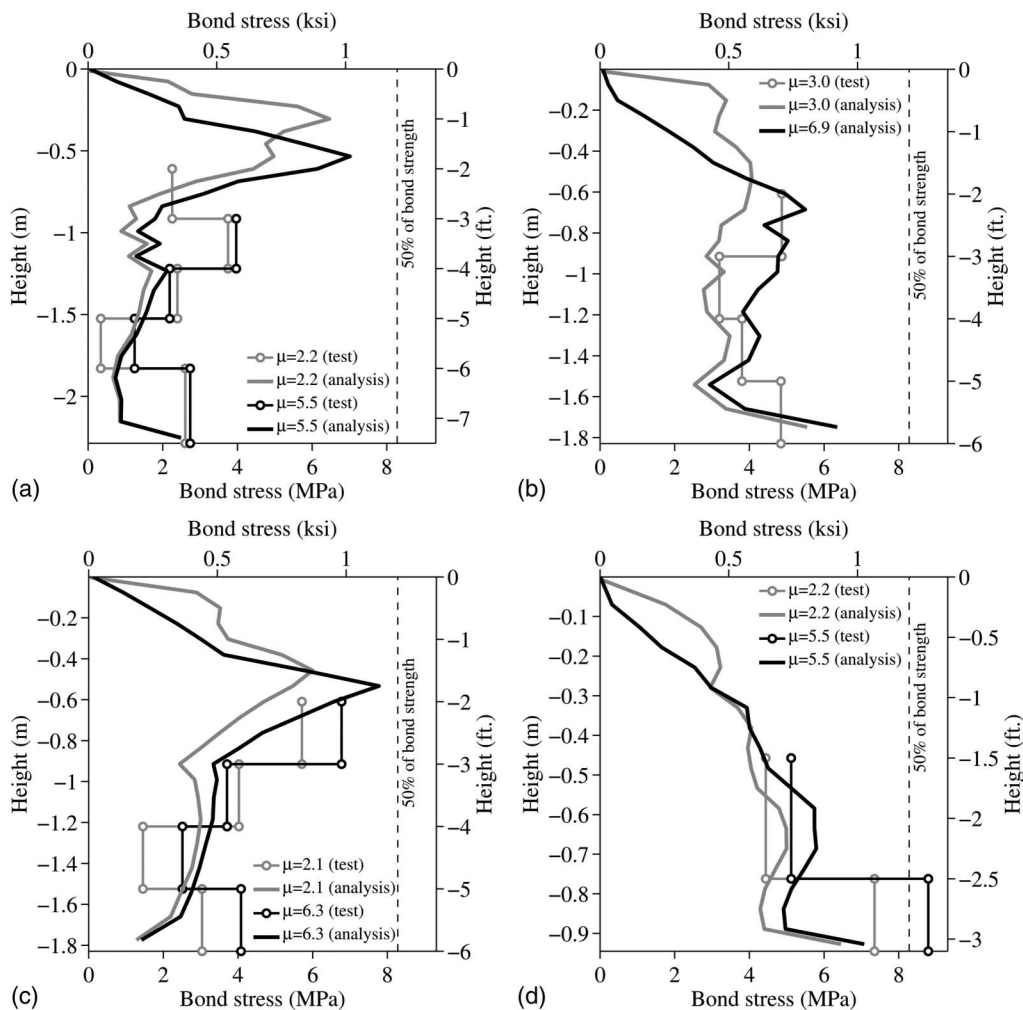
Fig. 10. Bond stresses along the anchorage of the column longitudinal bar at the north face of the specimens: (a) Specimen 1; (b) Specimen 2; (c) Specimen 3; (d) Specimen 4

Once the bar yields, the bond resistance deteriorates. At $\mu = 5.5$, most of the bond resistance is provided in a region between 0.3 m (1 ft) and 1 m (3.3 ft) below the base of the column. In the remaining 2.3 m (4.2 ft) below this region, little bond resistance is

activated, with the bond stress less than 15% of τ_{max}, because the bar does not slip much in this lower region. This indicates that a significant portion of the embedment length is not used to develop the bar stress.

Fig. 11. Bar slip along the anchorage of the column longitudinal bar at the north face of Specimens 1 and 4: (a) slip along the entire anchorage; (b) close-up view of slip along the lower portions of the anchorage

As shown in Figs. 10(b and d), Specimens 2 and 4 have different bond-stress distributions along the column longitudinal bars as compared with Specimen 1. These specimens have reduced embedment lengths of $l_d + s + c$. For these specimens, the bond resistance along the upper $15d_b$ of the embedment lengths has deteriorated significantly when the displacements are at the maximum reached in the tests. Along the remaining bar embedment lengths, the bond stresses are more or less uniform and remain below 40% of τ_{max}. These results indicate that the bars have experienced more slip, and the bond resistances along the entire embedment lengths are more fully mobilized, with little extra anchorage capacity.

Fig. 10(c) shows that the use of the steel casing around the pile in Specimen 3 has resulted in bond-stress distributions similar to those for Specimen 1, even though it has the same embedment length as Specimen 2. The peak bond stress reached is even higher than that for Specimen 1. These results indicate the benefit of added confinement caused by the steel casing.

The slips of the bars at the north face of Specimens 1 and 4 along the anchorage zones are plotted in Fig. 11. The slips are much larger in the upper regions of the anchorage zones where the bars have yielded. Below the plastic strain regions, the bar slips are significantly smaller than s_{peak}, which is the slip at which the peak bond strength τ_{max} would be attained if the bar were to remain elastic and slip monotonically in one direction. Specimen 4 has a larger slip in the lower portion of the bar than Specimen 1. This explains why Specimen 4 has larger bond stresses mobilized in the lower portion of the bar than Specimen 1.

### Strains in the Transverse Reinforcement of the Piles

Fig. 12 compares the numerical and experimental results on the strains in the transverse reinforcement of the piles at the south face of the specimens. These strains are the result of the splitting forces caused by bar slip and the prying action of the column in the pile. As shown in Fig. 12(a), for Specimen 1, the FE model tends to overestimate the strains in the hoops near the top of the pile. Otherwise, the agreement is satisfactory. For Specimen 2, the maximum strain in the uppermost hoop is slightly underestimated by the FE model. In addition, the increase of hoop strains between $\mu = 2.0$ and $\mu = 5.0$ predicted by the FE model is smaller than that measured in the tests. Similar conclusions can be drawn for the transverse reinforcement and the steel casing in Specimen 3, as shown in Figs. 12(c) and 13, respectively. The hoop strain profile

obtained for Specimen 4 by the FE model is similar to that for Specimen 2, as shown in Fig. 12(d). Nevertheless, the test results show very large hoop strains at an elevation that is 0.64 m (2.1 ft) below the top of the pile. Wider splitting cracks were also observed at this location during the test, as compared with the other specimens. This can be attributed to the prying action of the column, which is probably not well captured by the FE model.

Fig. 14 shows the plots of the lateral load applied to the column versus the strain obtained at the south side of the first hoop from the top of the pile in Specimen 2. The test results show that the hoop strain at the south side increased when the top of the column was displaced toward the south (positive direction) or toward the north, and decreased when the column was unloaded. The strain increase was largely caused by the splitting forces induced in the concrete by bar slip when the bar was pulled from or pushed into the pile as explained in Murcia-Delso et al. (2016). Furthermore, the test result shows that the hoop strain developed in later cycles at the south side was higher when the column was displaced toward the south than toward the north. This can be partly attributed to the lateral plastic dilatation of the concrete, as it was compressed, and partly to the prying action of the column. However, the FE model shows that a different behavior in that the hoop strain near the south face increases only when the column is loaded toward the south and the hoop strain does not drop after unloading. For this reason, the increase of hoop strains with the ductility demand is more rapid for the FE model as compared with the tests, as depicted in Figs. 12(b) and 14. Nevertheless, the maximum hoop strain developed is smaller than that in the test. These differences can be attributed to a number of factors, including the deficiency of the concrete model in representing the closing of the splitting cracks after the reversal in bar slip, the underestimation of the splitting force in the bond-slip model as the bond stress deteriorates, and the inability of the FE model to accurately capture the prying action. The same observations have been obtained for the hoop strain at the north side and for the other specimens.

Numerical Study of the Margin of Safety of the Reduced Embedment Length

Both of the large-scale column-pile tests reported in Murcia-Delso et al. (2016) and the FE analyses presented in the previous section provide strong evidence that an embedment length of $l_d + s + c$ is
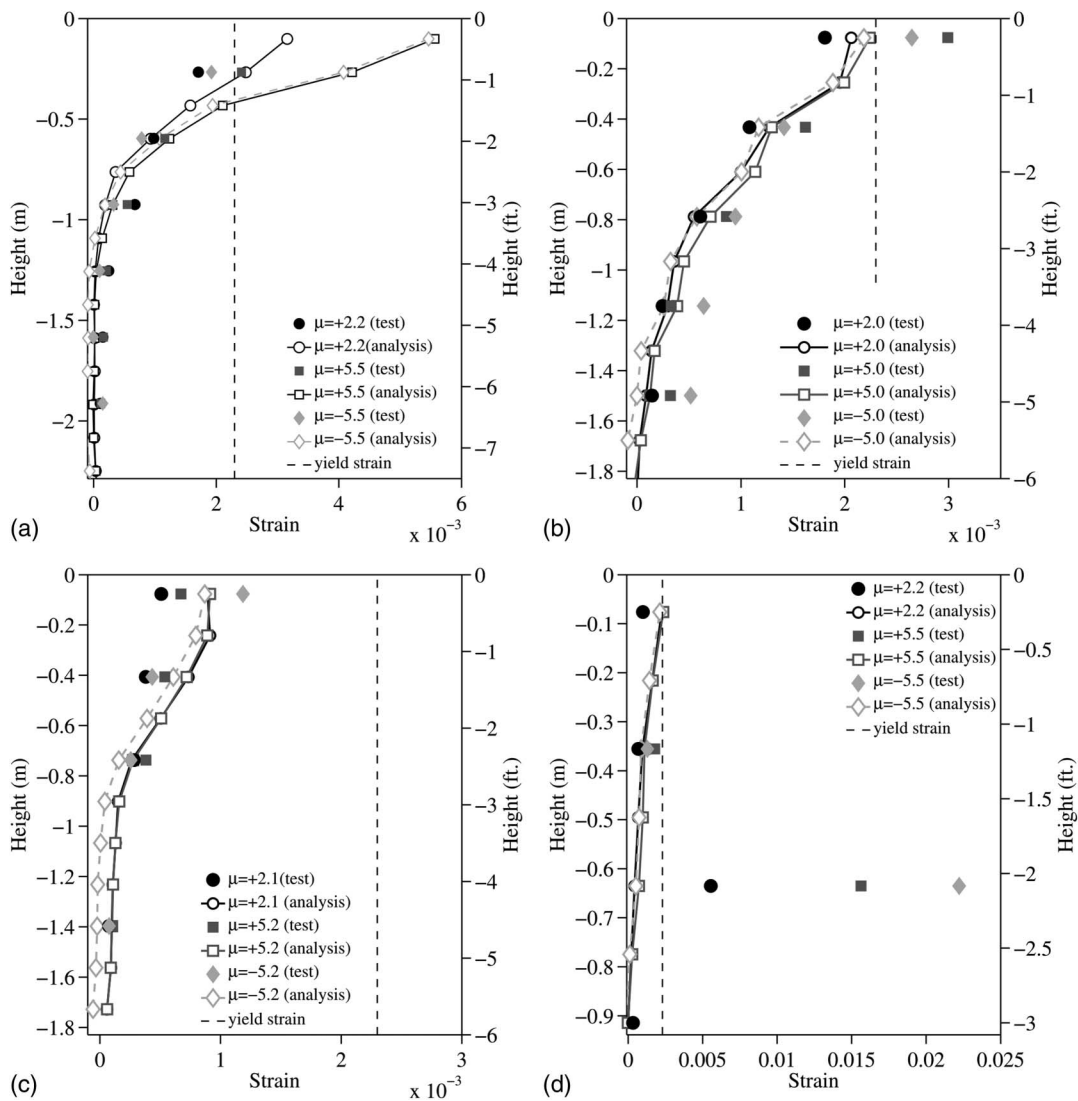
Fig. 12. Strains in pile hoops at the south face of the specimens: (a) Specimen 1; (b) Specimen 2; (c) Specimen 3; (d) Specimen 4
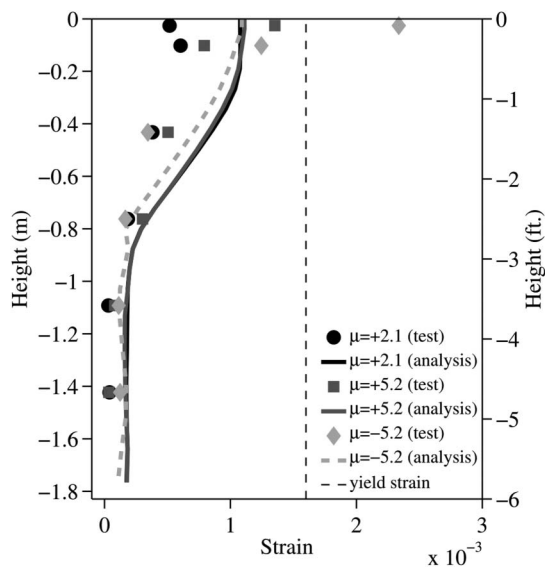

Fig. 13. Hoop strains in steel casing at the south face of Specimen 3
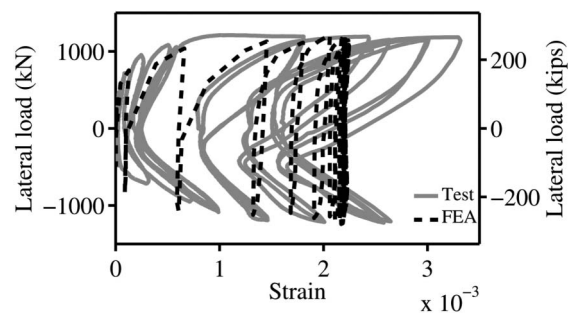
Fig. 14. Strains in pile hoop at 76 mm (3 in.) below the top of the pile at the south face of Specimen 2

sufficient to prevent the anchorage failure of the column longitudinal bars, allowing the development of the full flexural capacity of the column. Except for Specimen 3, which had a steel casing around the pile, the FE analyses have also shown that significant bond stresses develop near the end of the embedment length of
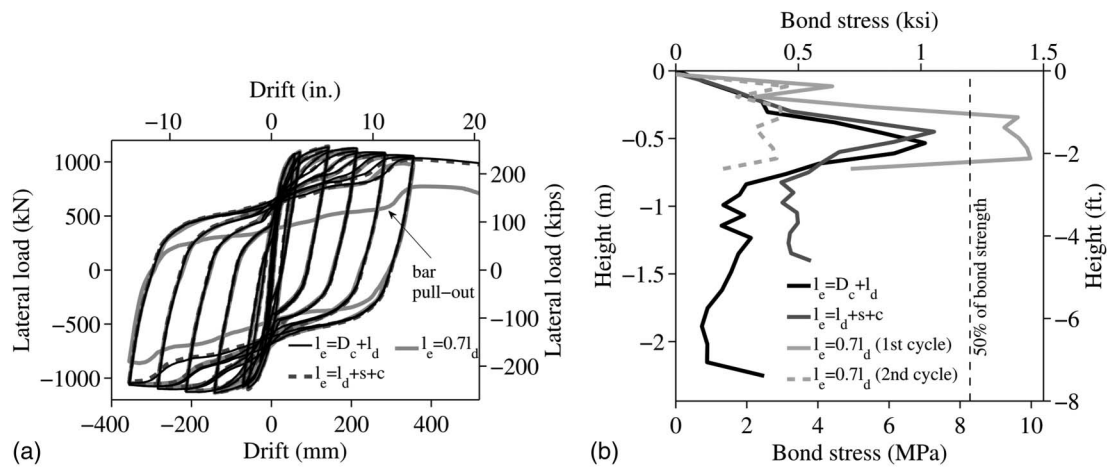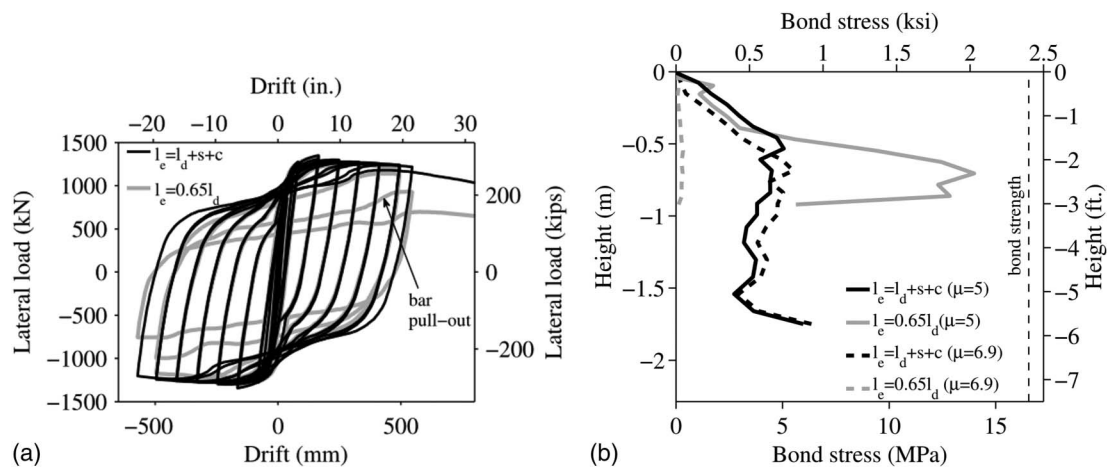
Fig. 15. Analysis results for Models 1a, 1b, and 1c: (a) lateral force versus drift; (b) bond stresses along the anchorage of the column longitudinal bar at the north face of the pile at $\mu = 5.5$

$l_d + s + c$, which indicates that there is little reserve bond capacity. To confirm that the above observations are true in general for column-pile assemblies of different cross-sectional dimensions and reinforcing details, and identify the margin of safety against bond failure with the aforementioned embedment length, a numerical study has been conducted with FE models. In this study, seven additional column-pile assemblies were analyzed. Their design is provided in Table 1 and they are divided into groups according to the column and pile diameters and design details. Group 1 has the column and pile diameters and the longitudinal reinforcement identical to those of Specimen 1 (which is designated as Model 1a), whereas Group 2 has the properties identical to those of Specimen 2 (which is designated as Model 2a). Groups 5 through 7 have larger diameter columns and piles. The models in each group have different embedment lengths for the column longitudinal bars. In addition, the transverse reinforcement in the bar anchorage region of the piles in Models 1b and 1c is slightly higher than that in Model 1a to satisfy the requirement proposed by Murcia-Delso et al. (2016) to prevent premature bond failure that could be caused by the splitting of concrete. The properties of the concrete, steel, and bond-slip model used in these analyses are the same as those for the test specimens, as presented in Table 2. In the analyses, the columns are subjected to the same cyclic loading

protocol as the test specimens, except that an extra half cycle is added at the end to impose a large displacement ductility demand of 10 to ensure that the bond is fully exercised.

Fig. 15(a) compares the lateral force–versus–displacement hysteresis curves for the models in Group 1. Models 1a and 1b, which have $l_e = D_{c,\max} + l_d$ and $l_e = l_d + s + c$, respectively, have almost identical hysteresis curves, whereas Model 1c, which has the shortest embedment length of $0.7l_d$, has several column longitudinal bars pulled out from the pile during the second cycle at $\mu = 5.5$. The pull-out failure of the bars causes a significant decrease of the lateral load-carrying capacity, as shown in Fig. 15(a). Additional analyses, which are not reported in this paper, have shown that pull-out failure will not occur for embedment lengths longer than $0.7l_d$. The bond-stress profiles along the embedment length of the column longitudinal bars at the north face of Models 1a to 1c at $\mu = 5.5$ are plotted in Fig. 15(b). As shown, a reduction of the embedment length to $0.7l_d$ results in a much higher bond-stress demand over the entire embedment length in the first cycle and a significantly reduced bond resistance in the second cycle because of the severe bar slip, which leads to bond failure.

Fig. 16 compares the results for Models 2a and 2b. Model 2b replicates Specimen 2 but has a reduced embedment length of $l_e = 0.65l_d$. This model has a bar pull-out failure exhibiting
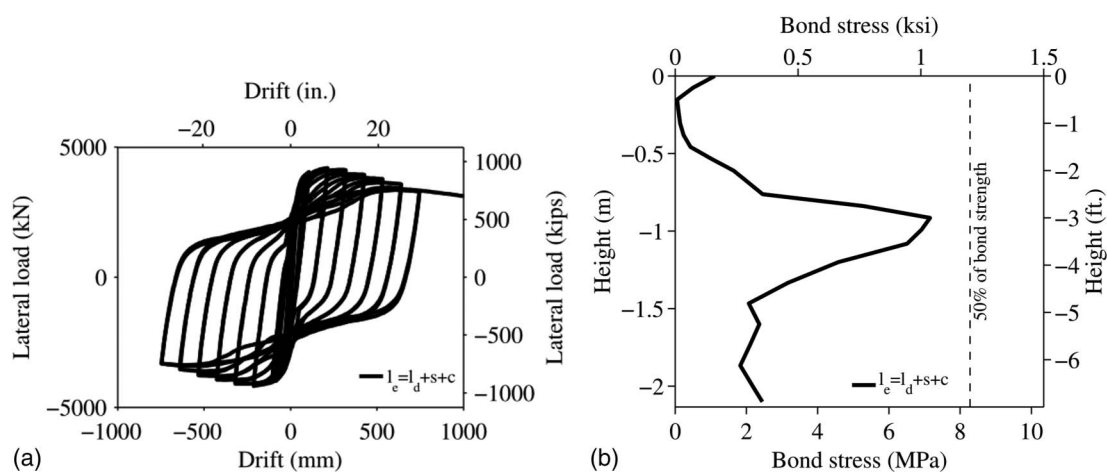

Fig. 16. Analysis results for Models 2a and 2b: (a) lateral force versus drift; (b) bond stresses along the anchorage of the column longitudinal bar at the north face of the pile
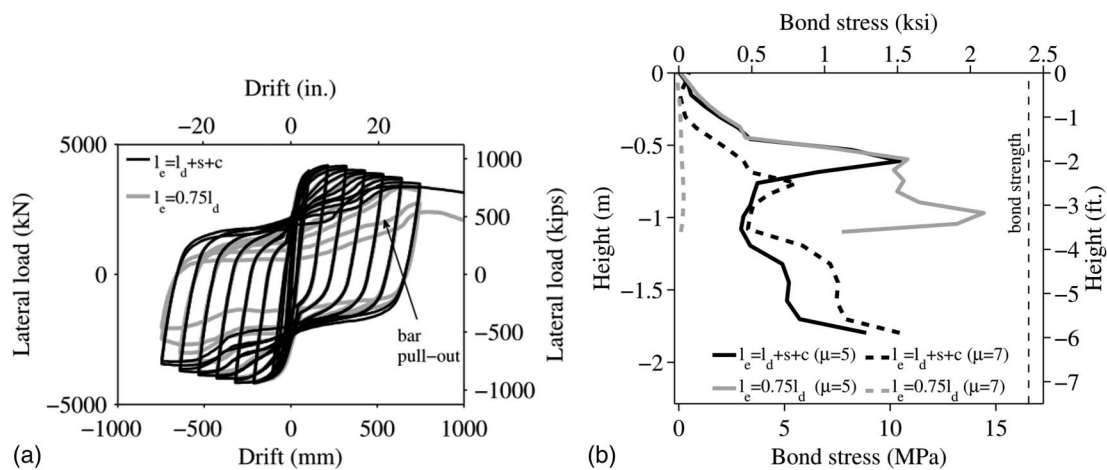
Fig. 17. Analysis results for Models 5a and 5b: (a) lateral force versus drift; (b) bond stresses along the anchorage of the column longitudinal bar at the north face of the pile

Fig. 18. Analysis results for Model 6: (a) lateral force versus drift; (b) bond stresses along the anchorage of the column longitudinal bar at the north face of the pile at $\mu = 7$

significant load degradation under cyclic loading, as shown in Fig. 16(a). Fig. 16(b) shows a very high bond-stress demand for $l_e = 0.65l_d$, which quickly leads to bond failure. For embedment lengths longer than $0.65l_d$, pull-out failure does not occur as indicated by additional analyses, which are not reported in this paper. The bond stress distributions plotted for the shorter embedment length in Fig. 16(b) also indicate that the development of large bond stresses near the bottom end of the anchorage can be quickly followed by bond failure.

Results for the models that have a larger column diameter of 2,438 mm (8 ft) are presented in Figs. 17 and 18. The column longitudinal reinforcement for Model 5a has an embedment length of $l_d + s + c$ in a pile of diameter equal to 3,048 mm (10 ft). The response of this model is compared with that of Model 5b, which has the embedment length reduced to $l_e = 0.75l_d$. Model 5b has the pull-out failure of the bars. For embedment lengths longer than $0.75l_d$, pull-out failure does not occur, as indicated by additional FE analyses. Even though bar pull-out failure does not occur in Model 5a, the bond stress at the bottom of the embedment length is very high, as shown in Fig. 17(b), indicating large bar slip at the end. This bond-stress distribution and the fact that the threshold

embedment length of $l_e = 0.75l_d$ for bar pull-out failure is longer than that of the other models suggest that Model 5a has a lower safety margin. This can be attributed to the smaller pile-to-column diameter ratio, which results in more severe cracking in the pile. This observation is also supported by the experimental and numerical results obtained for Specimen 4, which had the same pile-to-column diameter ratio.

Models 6 and 7, which have column and pile diameters equal to 2,438 mm (8 ft) and 3,658 mm (12 ft), and $l_e = l_d + s + c$ perform satisfactorily. As shown in Fig. 18, Model 6 does not show any load degradation in the force-displacement curves other than that caused by the P-delta effect of the vertical load, and the bond stress peaks at a location far from the bottom end of the bar. Hence, increasing the ratio of the pile diameter to the column diameter introduces a higher margin of safety against bar pull-out failure. Similar results have been obtained for Model 7.

Conclusions

This paper presents nonlinear FE analyses to study the bond behavior and the development of column longitudinal reinforcement

extended into oversized pile shafts. The numerical results show that the embedment length specified in the AASHTO LRFD Seismic Bridge Design Specifications (AASHTO 2011) and the Caltrans Seismic Design Criteria (Caltrans 2010) for column longitudinal bars extended into an oversized pile shaft is very conservative, and that the reduced embedment length of $l_e = l_d + s + c$ that was recommended in Murcia-Delso et al. (2016) has a good margin of safety against pull-out failure of the column bars. For piles that have the minimum transverse reinforcement recommended in Murcia-Delso et al. (2016) and a minimum pile-to-column diameter ratio of 1.25, the reduced embedment length is at least 1.33 times the length required to prevent bar pull-out failure based on the numerical results presented in this study.

Results of the FE analyses indicate that using an engineered steel casing for additional confinement improves the bond performance and reduces the slip of the column longitudinal bars in the pile. The numerical results have also confirmed the experimental observations in Murcia-Delso et al. (2016) that the performance of the bar anchorage in an oversized pile shaft depends on the ratio of the pile diameter to the column diameter. Bar anchorage capacity appears to be weaker, and more severe cracking is observed in the pile when the ratio of the pile diameter to the column diameter decreases. A larger pile diameter–to–column diameter ratio provides a better confinement to control radial splitting cracks induced by bar slip and the prying action of the column.

Acknowledgments

References

AASHTO. (2010). *LRFD bridge design specifications*, 5th Ed., Washington, DC.

AASHTO. (2011). *Seismic bridge design specifications*, 2nd Ed., Washington, DC.

Abaqus version 6.10 [Computer software]. Dassault Systemes Simulia, Providence, RI.

ASTM. (2009). "Standard specification for low-alloy steel deformed and plain bars for concrete reinforcement." *ASTM A706/A706M-09b*, West Conshohocken, PA.

Caltrans (California Department of Transportation). (2010). *Caltrans seismic design criteria, version 1.6*, Sacramento, CA.

Karthik, M. M., and Mander, J. B. (2011). "Stress-block parameters for unconfined and confined concrete based on a unified stress-strain model." *J. Struct. Eng.*, 10.1061/(ASCE)ST.1943-541X.0000294, 270–273.

Lee, J., and Fenves, G. L. (1998). "Plastic-damage model for cyclic loading of concrete structures." *J. Eng. Mech.*, 10.1061/(ASCE)0733-9399 (1998)124:8(892), 892–900.

Lubliner, J., Oliver, J., Oller, S., and Oñate, E. (1989). "A plastic-damage model for concrete." *Int. J. Solids Struct.*, 25(3), 299–326.

McLean, D. I., and Smith, C. L. (1997). "Noncontact lap splice in bridge column-shaft connections." *Rep. No. WA-RD 417.1*, Washington State Transportation Center, Washington State Univ., Pullman, WA.

Moharrami, M., and Koutromanos, I. (2016). "Triaxial constitutive model for concrete under cyclic loading." *J. Struct. Eng.*, 10.1061/(ASCE)ST .1943-541X.0001491, 04016039.

Murcia-Delso, J., Liu, Y., and Shing, P. B. (2016). "Development of bridge column longitudinal reinforcement in oversized pile shafts." *J. Struct. Eng.*, 10.1061/(ASCE)ST.1943-541X.0001591, 04016114.

Murcia-Delso, J., and Shing, P. B. (2015). "Bond-slip model for detailed finite element analysis of reinforced concrete structures." *J. Struct. Eng.*, 10.1061/(ASCE)ST.1943-541X.0001070, 04014125.

Murcia-Delso, J., Shing, P. B., Stavridis, A., and Liu, Y. (2013). "Required embedment length of column reinforcement extended into type II shafts." *Rep. No. SSRP–13/05*, Structural Systems Research Project, Dept. of Structural Engineering, Univ. of California, San Diego.

Murcia-Delso, J., Stavridis, A., and Shing, P. B. (2015). "Tension development length of large-diameter bars for severe cyclic loading." *ACI Struct. J.*, 112(6), 689–700.